Nanoscale

ROYAL SOCIETY OF CHEMISTRY

PAPER

View Article Online
View Journal | View Issue

Check for updates

Cite this: *Nanoscale*, 2025, **17**, 15231

Mechanism for spiral growth of β-antimonene on a pitted substrate: vacancy line aggregation triggered by nanoscale step-loops†

Wenmin Li,[a] Hao Hu*[b] and Yi Pan *[a]

Received 18th February 2025,
Accepted 26th May 2025

DOI: 10.1039/d5nr00728c

rsc.li/nanoscale

The rising new field of twistronics, which is centered on the mechanically twisted multilayers of two-dimensional materials (2DMs), is in need of direct growth methods for the desired samples. Here, we present a comprehensive strategy for synthesizing twisted multilayer 2DMs *via* a spiral growth mode. This strategy is based on a first-principles calculations investigation of β-antimonene (β-Sb) on a pitted Ge(111) substrate surface with step-loops. Building on previous experimental observations, we have developed a theoretical model that elucidates the growth mechanism of the twist spiral structure. Our findings reveal that the step-loops play a crucial role in maintaining the lattice-mismatch-induced compressive strain in the β-Sb. As this strain accumulates, a vacancy line is inevitably formed in the first layer, facilitating the spiral dislocation in the second layer. It is also confirmed that the formation energy of the vacancies in β-Sb is lower in the high compressive strain state, and these vacancies tend to aggregate and form a linear structure. The kinetic study reveals a lower energy barrier for vacancy migration in the high compressive state. This theory presents a detailed growth mechanism for the spiral-assisted twist structure of 2D materials, which would be candidate samples for twistronics.

1. Introduction

Since the first successful preparation of graphene by the mechanical exfoliation method in 2004,[1] the stacking order, twist angle, and thickness of two-dimensional layered materials can be artificially modulated to realize distinctive properties such as superconductivity,[2] moiré excitons,[3] and high-performance catalysts.[4] In particular, many efforts have been devoted to changing the angle of interlayer twisting to form a moiré pattern with a magic angle, resulting in optical,[5] photocatalytic[6] and quantum effects;[7–9] this field has recently come to be known as "twistronics".[10] For example, the bilayer magic angle graphene successfully realized in 2018 has demonstrated unconventional superconducting properties.[2] Nonetheless, it is still challenging to achieve layered materials with multi-layer twist through artificial stacking or controlling the relative orientation growth of the layers.[11–13] The bottom-up growth method has begun to draw attention, as it can be used to produce twisted spiral multilayer materials directly by adjusting the number of growth layers and the angle of twist accurately and is more suitable for mass production.[5,6] The peculiar Eshelby twist of one-dimensional nanowires has been theoretically and experimentally observed.[14,15] However, the twist angle is inversely proportional to the cross-sectional area, which makes it challenging to apply this mechanism to 2D materials with high specific surface areas.[16,17] The bottom-up growth methods for twisted two-dimensional materials require further exploration.

2D layered materials are usually grown in a layer-by-layer manner,[18,19] while spiral-dislocation-driven growth can induce a continuous layered structure like a circular winding staircase.[20,21] According to the Burton–Cabrera–Frank (BCF) theory of classical crystal growth, after a linear defect shears a layered material, the new layer continues to grow from the edge of the crack to form a spiral dislocation until it grows into a continuous spiral layer.[20,22] For example, when two domains of WSe_2 intersect, a boundary will rise on one side, and there will be unsaturated Se atoms at the rising edge. The subsequent sources will either be added to the transverse edge to form transverse growth or added to the rising edge to create a second layer with a screw dislocation, which further promotes the growth of helical WSe_2.[23] Similarly, a screw dislocation caused by a domain boundary leads to the formation of double spiral hexagonal BN.[24] Screw dislocation defects are

---

[a] Center for Spintronics and Quantum Systems, State Key Laboratory for Mechanical Behavior of Materials, Xi'an Jiaotong University, Xi'an 710049, China. E-mail: yi.pan@xjtu.edu.cn

[b] Luology(Shandong) Digital Technology Co., LTD., Weifang 261021, China. E-mail: hao_hu@luology.com

† Electronic supplementary information (ESI) available. See DOI: **https://doi.org/10.1039/d5nr00728c**

generated in layered MoS_2 by introducing a sulfur saturation peak at the initial stage of the reaction during chemical vapor deposition (CVD).[25] Controlling the supersaturation concentration of precursors is a common dynamic practice to obtain spiral structures according to the screw dislocation growth theory.[22–28]

Conversely, templatization of the substrate surface enables the layered material to introduce screw dislocation during nucleation growth, or even to form supertwisted spiral layers. Using the physical vapor deposition (PVD) method, the introduction of atomic-scale steps on the substrate surface can induce SnS to cross the steps, forming screw dislocations at the edges. This process results in the formation of spiral SnS nanosheets with a high yield of 90%.[29] In another approach, the substrate surface is modified by introducing a protrusion, thereby creating a non-Euclidean surface. This modification drives the formation of twisted spirals through the screw dislocation mechanism.[30,31] Recently, the J. Zhang group reported that spiral β-Sb islands could form on an arsenic-saturated Ge(111) surface with step-loops.[32] Each spiral is evolved from a screw dislocation nucleated exactly at the center of a step-loop, which implies the atomic level step-loop triggers the desired spiral 2D layered material. The twist spiral structure grown inside the step-loops is similar to the screw-dislocation-driven spiral structure generated on the non-Euclidean surface.[30] However, the atomic-level mechanism and a general criterion that determines spiral formation are still lacking.

In this paper, inspired by the experimental observation of spiral β-Sb on As-saturated Ge(111) with step-loops, we systematically studied the influence of step-loops on the morphology and structure of the 2DM on the substrate surface. Structure models of monolayer β-Sb grown on a Ge(111) substrate surface with 1 × 1 As terminals under different strain conditions have been established. By comparing the formation process of β-Sb line defects on step-loop and flat surfaces, we demonstrate the mechanism of the growth of the spiral layered structure caused by the step-loops on the substrate surface from both thermodynamic and kinetic perspectives. Based on the calculation results, we propose a strategy for the epitaxial growth of twisted spiral-type layered materials on substrates with nanoscale step-loops, and the kinetic growth factors included precursor concentration. Our study would build a solid foundation for the facile production of vdW spiral materials for device application in twistronics.

2. Modeling and calculation method

The presence of step-loops on the substrate surface is a critical factor in determining the formation of spiral structures, as their size and depth can significantly influence the morphology of films nucleated within these loops. Thus, we propose growth models for different morphologies of 2D materials on a substrate surface. When nucleation and growth of 2D materials occur at the edge of the step-loop and on the flat surface of the substrate, they will experience varying degrees of planar lattice mismatch strain, leading to the formation of a spiral structure with a twist angle and a layered structure, as shown in Fig. 1a.

We investigated the most stable structures of As/Ge substrates and β-Sb grown on the As/Ge substrate surface, and the formation and migration of vacancies in the antimonene grown in the step-loops and on the flat terrace surface of the As/Ge(111) substrate. Firstly, we simulated the substrate structure and calculated four structures of As adsorbed on Ge(111) surfaces, including top, bridge, HCP hollow, and FCC hollow, with one As atom per unit cell to interact with the dangling bonds of the Ge(111) surface. Secondly, we studied the interaction between antimonene and the As/Ge substrate. Two Sb atoms per unit cell were placed on bridge–bridge, top–HCP hollow, top–FCC hollow or FCC hollow–HCP hollow locations on the stable As/Ge substrate. Considering the relative height of two Sb atoms, seven conditions were calculated to obtain the most stable growth position of β-Sb on the As/Ge(111) substrate surface. Finally, due to the large number of atoms in the As/Ge substrate, we removed it to simplify the model and explore the formation and migration of vacancies in 7 × 7 β-Sb. The formation energy and energy barrier of the vacancies in 7 × 7 supercell β-Sb were compared under two kinds of lattice mismatch compressive strain, and the calculation results show that the vacancies favor aggregation and line up under higher compressive strain in step-loops.

We used the Visualization for Electronic and STructural Analysis (VESTA) programme to construct the atomic structure models of Sb/As/Ge(111) and the β-Sb vacancy model, and observed the optimized structures to assess their validity.[33] The theoretical calculations were performed using the Vienna *ab initio* Simulation Package (VASP)[34] based on density functional theory (DFT) in a plane-wave basis set. The projector-augmented wave (PAW) method and the Perdew, Burke and Ernzerhof generalized gradient approximation (GGA-PBE) were utilized to describe the electron–nucleus and electron–electron interaction.[35,36] The van der Waals weak interactions were considered and treated using the DFT-D3 van der Waals correction with Becke–Jonson damping. The choice of the IBRION parameter for optimization was based on the actual structure. The convergence criteria of force between atoms and energy were set to 0.01 eV $Å^{-1}$ and 1×10^{-4} eV, respectively. The energy cutoff was set to 400 eV for all structures after testing. The Monkhorst–Pack scheme with 17 × 17 × 1 *k*-points was used as a grid sample in the Brillouin zone of the substrate structures. The CI-NEB method[37,38] was used to study the formation and migration of vacancies in β-Sb grown on the As/Ge(111) substrate. The influence of spin polarization induced by adsorption sites, heterojunctions, and vacancies on the spiral structure has not been considered in our study, as its contribution to the total structural energy is negligible, as shown in Tables S3 and 4.† Due to the large number of atoms in the substrate, we simplified the model after testing by utilizing a 7 × 7 monolayer supercell β-Sb structure and 3 × 3 × 1 *k*-points in the vacancy formation and migration calculations. All structure

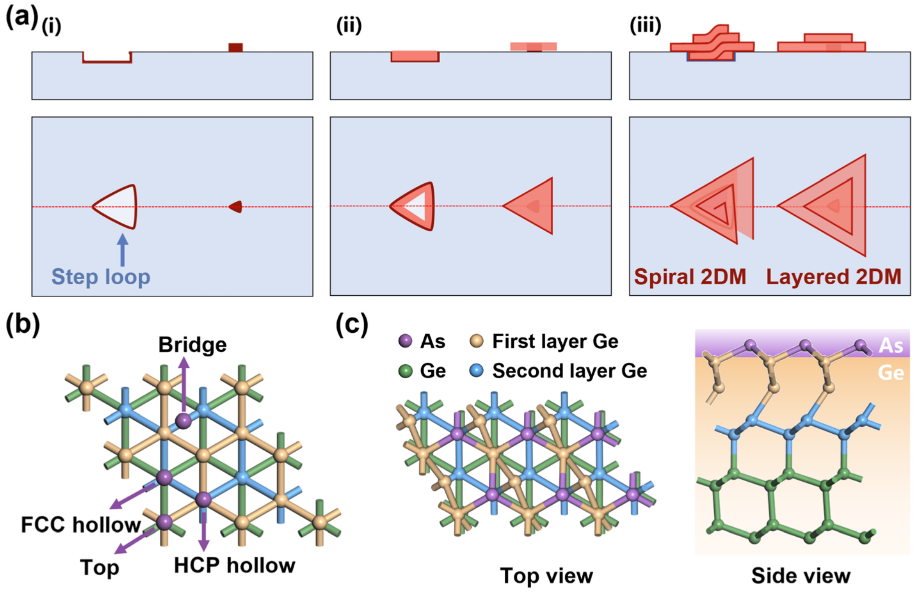

Fig. 1 Growth simulation of 2D materials with different morphologies on the substrate surface and As/Ge(111) substrate. (a) The two-dimensional material nucleates in the step-loop and on a flat region on the substrate surface (i), spreads and grows along the edge of the step and the nucleation center (ii), and finally forms a spiral structure with a twist angle and a layered structure (iii). (b) Supercell of the Ge(111) substrate and four kinds of initial As atom sites adsorbed on the Ge(111) surface. (c) Most stable adsorption configuration: the optimized structure of the As atom adsorbed at a bridge site and HCP hollow site.

models were constructed with a vacuum slab of about 20 Å to release the interaction between adjacent images.

3. Results and discussion

3.1. Atomic structure of β-Sb grown on the As/Ge(111) surface

There is one As atom adsorbed on each unit cell substrate. Four adsorption locations on the Ge(111) surface are considered, including top, bridge, HCP hollow, and FCC hollow (Fig. 1b). The As/Ge configuration energies of As atoms adsorbed on the bridge and HCP hollow are the same, and are the lowest among the four configurations, as shown in Fig. 1c (more details are provided in Fig. S1 and Table S1†). Three of the five electrons of the As atom form covalent bonds with three Ge atoms on the surface of the Ge(111) substrate, and the remaining two electrons form a lone pair of electrons, which is consistent with the literature.[39] Thus, an As/Ge(111) substrate surface without dangling bonds for the vdW epitaxial growth of β-Sb is obtained.

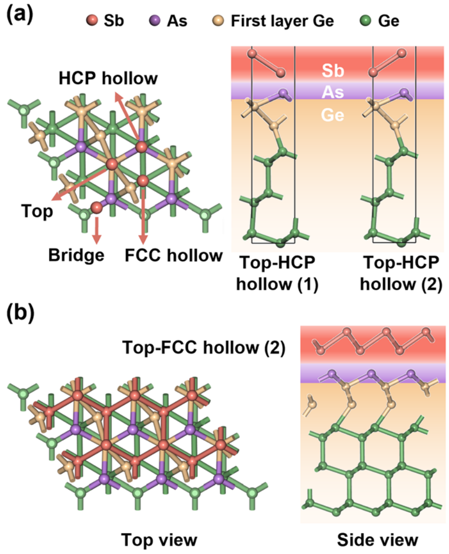

Fig. 2 β-Sb on As/Ge(111) substrate. (a) The two Sb atoms of β-Sb are located at different sites, *e.g.*, top–HCP hollow. (b) The most stable structure of the As/Ge substrates after optimization, in which the Sb atoms are adsorbed on the top–FCC hollow (2) sites.

One β-Sb unit cell was placed on one As/Ge(111) substrate unit cell, with the As atom located on the HCP hollow site of the Ge(111) surface. We considered the bridge, top, HCP hollow, and FCC hollow adsorption sites on the substrate surface as sites to place the two atoms of the β-Sb unit cell. For example, two Sb atoms placed on the top location and HCP hollow location create two situations due to the relative heights of the two atoms, which are tagged as top–HCP hollow (1) and top–HCP hollow (2) (Fig. 2a). For the bridge sites (top–bridge, HCP hollow–bridge, and FCC hollow–bridge), the bond length of β-Sb can adjust to 2.6, 3.4, or 3.85 Å, causing the lattice to undergo significant compressive or tensile strain. This also results in periodic matching issues with the substrate, which contrasts sharply with the actual β-Sb structure (Fig. S1d†). Thus, there are seven cases of Sb atoms situated on different As/Ge(111) sites, including the above cases and bridge–bridge, top–FCC hollow (1), top–FCC hollow (2), FCC hollow–HCP hollow (1) and FCC hollow–HCP hollow (2). The adsorption energy of β-Sb on the As/Ge(111) substrate surface is defined as:

$$\Delta E_{\mathrm{ad}} = E_{\mathrm{Sb/sub}} - E_{\mathrm{sub}} - E_{\mathrm{Sb}} \tag{1}$$

where $E_{\mathrm{Sb/sub}}$, E_{sub} and E_{Sb} are the energy for As/Ge(111) substrates with monolayer β-Sb, the As/Ge(111) substrates and β-Sb, respectively. The calculation adsorption results are shown in Table S1.†

The results demonstrate that β-Sb retains its original adsorption site in both the FCC–HCP hollow and top–FCC hollow configurations, with no observable relative diffusion of the Sb atoms. When β-Sb is placed in the other four adsorption conditions, it is found at the top–FCC hollow (2) site of the As/Ge(111) surface with the lowest adsorption energy (−0.69 eV) after optimization (more details are provided in Table S1†). This is the most stable structure of β-Sb on the As/Ge(111) surface (Fig. 2b).

The significant lattice mismatch between β-Sb and the As/Ge(111) substrate induces compressive strain. Notably, β-Sb grown within step-loop regions retains most of this strain due to geometric confinement at the step-loop boundaries. Conversely, β-Sb deposited on flat terrace surfaces exhibits partial strain relaxation enabled by unrestricted boundary conditions. This strain difference drives distinct growth morphologies: spiral structures in step-loops and multilayer stacking on flat terraces.

3.2. Linear aggregation of vacancies in β-Sb

A possible way to relax the strain is vacancy aggregation.[40] The lattice parameters of β-Sb and the Ge(111) substrate are 4.378 Å and 4.089 Å after structure optimization, and the mismatch is high at 7.07%. We used a 7 × 7 supercell structure to study the nature of the vacancies of β-Sb. Due to a large number of atoms of supercell substrates, which leads to slow calculations, and the fact that there is van der Waals interaction rather than a chemical bond between β-Sb and the As/Ge(111) substrate, we simplified the physical model by removing the substrate but retaining the strain *via* adjusting the lattice constant of β-Sb. We calculated the formation energy of vacancies for a 7 × 7 monolayer of β-Sb under high-lattice-mismatch compressive strain and low-lattice-mismatch compressive strain (the low strain is assumed to be about half the high strain), which correspond to β-Sb grown in the step-loop and on the flat terrace surface, respectively, and lattice parameters of the strained monolayer β-Sb are 4.089 Å and 4.25 Å respectively. The formation energy of n vacancies on a monolayer of perfect β-Sb with N Sb atoms is the difference of the structure energy of defective β-Sb with n vacancies and the energy of $(N - n)$ Sb atoms, which is defined as:

$$E_{\mathrm{n\ vcncy}} = E_{\mathrm{total}} - \left(\frac{N-n}{N}\right) E_{\mathrm{perf}} \tag{2}$$

where E_{total} and E_{perf} are the total energy of the 7 × 7 monolayer β-Sb lattice with n vacancies and perfect 7 × 7 monolayer β-Sb after optimization, respectively.

We calculated the formation energy for structures with one to six vacancies in the monolayer β-Sb. The configurations for each structure containing n (integer) vacancies were constructed based on the most stable structure with $(n - 1)$ vacancies. The calculated formation energies of these structures are listed in full in Table S2,† while the most stable configurations are displayed in Table 1. The single vacancy is indicated as A, while multiple vacancies are indicated as AB, ABC, ..., and so on. The different configurations of vacancies in β-Sb are distinguished by the numbers to the right of the letters, as shown in Fig. S2 and S3.† For example, the eight configurations of the two vacancies A and B are distinguished using AB_1, AB_2, ..., and AB_8 (Fig. 3a). The triple-vacancy structure ABC was studied based on the most stable AB configuration (Fig. 3b, the eight optimized configurations of AB are presented in Fig. S2†). It is found that the formation energy of a single vacancy under high strain is lower than that under low strain, indicating that structure defects of β-Sb are more easily formed on the pitted locations with large strain than the flat surface with miniscule strain. The formation energy of a single vacancy in β-Sb is 1.6473 eV ($\varepsilon \approx 7.07\%$), which is comparable to that of phosphorene (1.65 eV). However, at $\varepsilon \approx 3\%$, the formation energy is 2.1754 eV, which is higher than that of phosphorene. Nevertheless, both values are significantly lower than the single vacancy formation energy in graphene (7.57 eV).[41]

As shown in Fig. 3a, we considered eight double-vacancy configurations, ranging from those with the vacancies close to each other to those that are more distantly spaced. The configuration with the greatest distance, AB_8, resulted in two separate single-vacancy configurations upon optimization (double pentagon–nonagon; 59–59) (Fig. S2†). We believe that all possible configurations of the two vacancies in β-Sb have been considered. The AB_1 vacancy configuration with the closest distance has the lowest formation energy under both compressive strains (Fig. 3b). This indicates that the double vacancies tend to aggregate. Among them, AB_1 (pentagon–octagon–pentagon; 585) is the most stable, with formation energies of 1.7331 eV ($\varepsilon \approx 7.07\%$) and 2.5367 eV ($\varepsilon \approx 3\%$) (Table 1). This is different from the double-vacancy configurations in phosphorene (585-A: 1.41 eV > 5757-A: 1.35 eV) and graphene (555–777: 8.09 eV < 5555–6–7777: 8.69 eV < 585: 8.99 eV).[41] Notably,

Table 1 Formation energy of vacancies for monolayer 7 × 7 β-Sb with high and low strain

n	n vacancies	$\varepsilon \approx 7.07\%$ $E_{\mathrm{n\ vcncy}}$ (eV)	$\varepsilon \approx 3\%$ $E_{\mathrm{n\ vcncy}}$ (eV)
1	A	1.6473	2.1754
2	AB_1	1.7331	2.5367
3	AB_1C_2	2.7227	3.6422
4	$AB_1C_2D_4$	2.5897	4.0316
5	$AB_1C_2D_4E_3$	3.7494	5.0671
6	$AB_1C_2D_4E_3F_1$	3.9377	5.7612
	$AB_1C_2D_4E_3F_4$	4.7252	5.4291

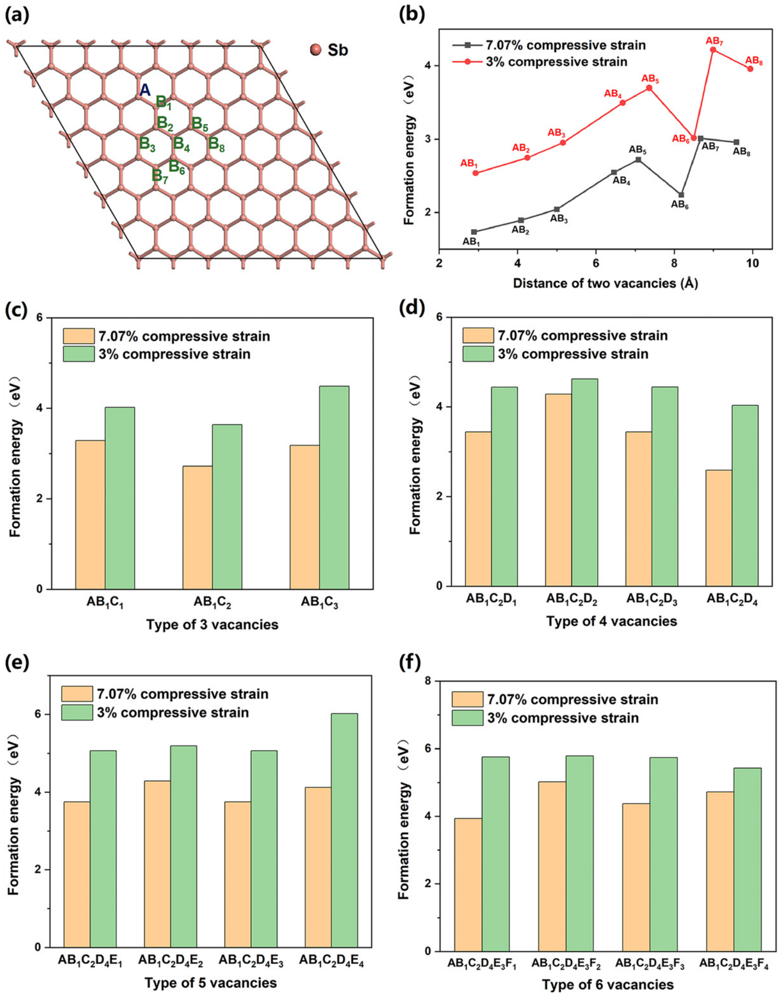

Fig. 3 Vacancy configurations of β-Sb under high and low strain, and comparison of their formation energies. (a) The eight double-vacancy configurations. (b) The energy for the formation of two vacancies varies with distance under both compressive strains. (c–f) Comparison of the formation energies of different configurations of triple- to sextuple-vacancies on β-Sb under 7.07% and 3% compressive strains.

the AB_6 configuration under 7.07% compressive strain has a low energy that does not follow the overall trend, which is probably because this structure is coincidentally more stable after optimization. However, its specificity is still in accordance with expectations, and its formation energy is higher than that of the most stable AB_1 configuration. The formation energies of three configurations of triple-vacancy AB_1C, which were obtained based on the most stable double-vacancy structure AB_1, were compared (Fig. 3c), and the most stable configuration AB_1C_2 was selected to study the structure of quadruple-vacancy β-Sb, *etc.*, until the sextuple-vacancy β-Sb was found to have a regular shape under high strain (Fig. 3d–f).

The relationship between the formation energy of the most stable vacancy configuration and the number of vacancies is shown in Fig. 4a (more configuration details are presented in Fig. S3†). The black line represents the formation energy of vacancies under 7.07% compressive strain, the red line represents the formation energy of vacancies under 3% compressive strain, and the dashed lines represent the formation energy of vacancies in dispersed discrete states. It can be concluded that the formation energy for a given number of vacancies under strain is lower than that for the same number of vacancies in discrete states, once again indicating that the vacancies tend to aggregate. Additionally, the formation energy for a given number of vacancies under the high strain value of 7.07% is lower than that under the low strain value of 3%, indicating that vacancy aggregations are formed more easily in β-Sb under high compressive strain. When there are six aggregated vacancies in β-Sb under the 7.07% high strain conditions, they form an ellipse (Fig. 4b), which is significantly different from the irregular shape of the six vacancies under 3% strain (Fig. 4c). Therefore, we have reason to assume that the aggregation of more vacancies will form a flatter oval, and that the vacancies will continue to aggregate and eventually arrange in a line, forming a line defect. The line defect will tear the β-Sb layer, causing a new layer to grow along the edge of the crack, creating a spiral structure.

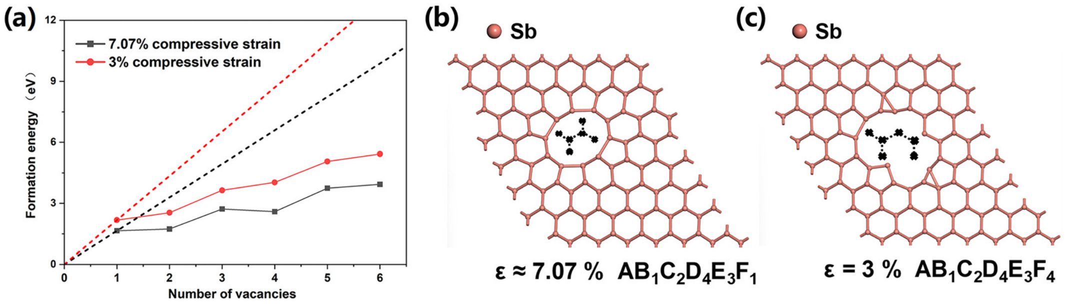

Fig. 4 (a) Formation energies of the most stable vacancy configurations as a function of the number of vacancies. (b and c) The most stable sextuple-vacancy configurations under (b) 7.07% strain: $AB_1C_2D_4E_3F_1$ and (c) 3% strain: $AB_1C_2D_4E_3F_4$.

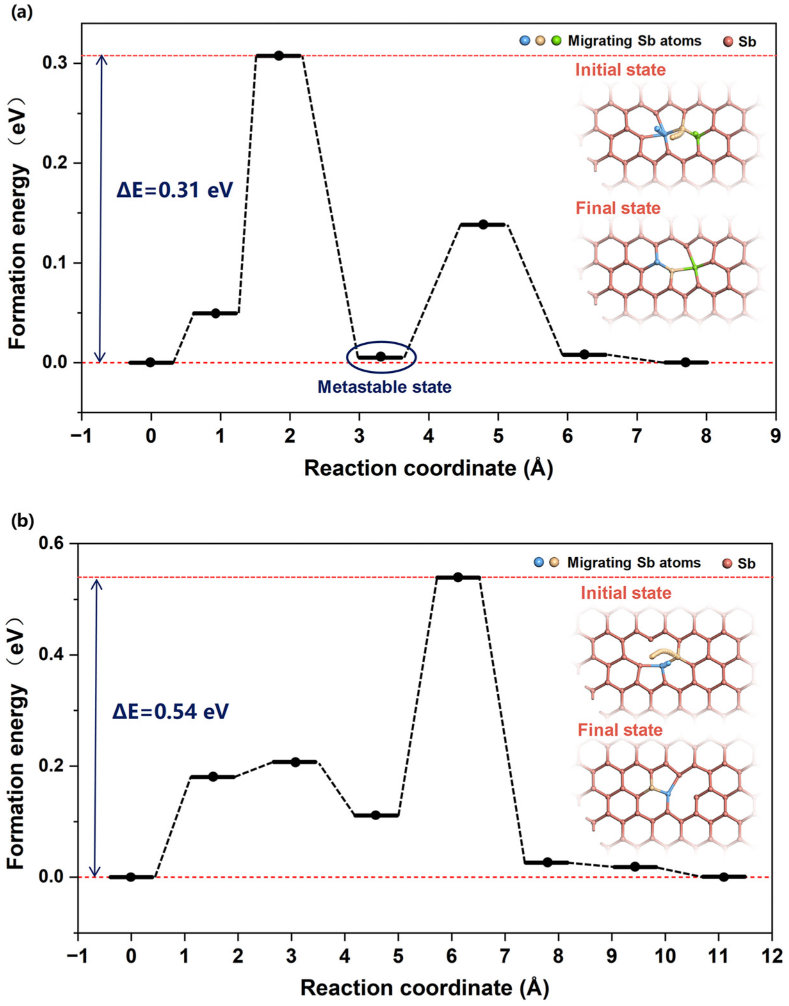

Fig. 5 Potential energy barrier of single vacancy migration under (a) 7.07% strain and (b) 3% strain. The migration trajectory is indicated in the inserted models.

3.3. Vacancy migration energy barriers

According to the previous works,[42,43] we used the CI-NEB method to calculate the potential energy barrier of single vacancy migration in 7 × 7 β-Sb under 7.07% strain and 3% strain (Fig. 5). The migration energy barrier of the vacancy under 7% strain is $\Delta E_{7.07\%}$ = 0.3075 eV, which is obviously much lower than the migration energy barrier $\Delta E_{3\%}$ = 0.5385 eV under 3% strain, indicating that vacancies are more prone to migration and aggregation under high strain. The structural changes in the transition state of β-Sb during the single vacancy migration under the two kinds of strains are demonstrated in Fig. S4 and Fig. S5.† Additionally, it is evident that there is a metastable structure when the single vacancy on β-Sb migrates under 7.07% strain, with a relatively low energy of ~4 meV compared to the energy of the initial and final states. However, it is still a transitional state through which a single vacancy structure evolves.[44]

We only studied the aggregation of one to six vacancies due to computational speed; the aggregation of more vacancies into line defects would require extensive computational observations. However, these calculations can provide sufficient evidence for our theory and confirm its reliability. This is consistent with previous experimental observations, in which screw dislocations were found to tend to aggregate in different regions.[45] In addition, we only studied the first layer of helical β-Sb to form the screw dislocation seed; the second or additional layers of β-Sb were not simulated. The band structure analysis of spiral β-Sb is presented in the ESI.† The possible physical, optical, and piezoelectric properties of spiral β-Sb are yet to be further explored *via* simulation.[23,25,29]

Step-loops with specific sizes are constructed on the surface of the substrate, and the edge of the step is conducive to the formation of β-Sb nucleation sites.[46,47] The lattice mismatch between the β-Sb and the As/Ge(111) substrate induces strain, which is retained at the step-loop boundary. This strain results in the formation of screw dislocations, driving spiral growth instead of classic layer-by-layer growth.[46,48] Based on this, the growth model indicates that controlling the size and depth of the step-loop, which modulates the curvature of the indentation, can regulate the spiral structure with a twisting angle, producing fastened supertwisted spiral layered materials (see discussion in Fig. S8†). These spiral structures are pinned within the step loops, enabling position-controlled fabrication. This theoretical model is consistent with the explanation proposed by previous researchers for the screw-dislocation-driven spiral structures caused by line defects.[5,21–26,30,31]

4. Conclusions

We take the formation of different β-Sb growth structures on the surface of a germanium substrate as an example to verify one condition for the formation of spiral-structure 2D layered materials on a semiconductor substrate: the construction of nano-scale step-loops on the substrate surface. We propose a strategy for the growth of spiral layered materials, which suggests that the step-loop retains the lattice mismatch compressive strain between the layered material and the substrate, and that the spiral structure is the result of screw dislocation growth as the vacancies line up into line defects under this compressive strain. Additionally, we suggest that the step-loop has a minimum critical size to form a spiral structure, and increasing the depth to the nanometer scale and reducing the diameter of the step-loop will form a super-twisted fastened spiral structure. These conclusions and predictions require further experimental and theoretical verification and exploration. Our calculations and theories provide a new strategy for synthesizing twist spiral 2D materials that would find applications in twistronics.

Author contributions

Wenmin Li: investigation, software, methodology, data curation, visualization, writing – original draft. Hao Hu: conceptualization, methodology, formal analysis, resources, supervision. Yi Pan: validation, formal analysis, resources, project administration, funding acquisition, supervision, writing – review & editing.

Data availability

All data of this study are comprehensively presented in the Results and discussion section and the ESI.†

Conflicts of interest

There are no conflicts to declare.

Acknowledgements

This work was financially supported by the National Key Research and Development Program of China (Grant No. 2022YFA1204100), the National Natural Science Foundation of China (Grant No. 12074302) and the Strategic Priority Research Program of the Chinese Academy of Sciences (Grant No. XDB30000000).

References

1 K. S. Novoselov, A. K. Geim, S. V. Morozov, D. Jiang, Y. Zhang, S. V. Dubonos, I. V. Grigorieva and A. A. Firsov, *Science*, 2004, **306**, 666–669.

2 Y. Cao, V. Fatemi, S. Fang, K. Watanabe, T. Taniguchi, E. Kaxiras and P. Jarillo-Herrero, *Nature*, 2018, **556**, 43–50.

3 K. L. Seyler, P. Rivera, H. Yu, N. P. Wilson, E. L. Ray, D. G. Mandrus, J. Yan, W. Yao and X. Xu, *Nature*, 2019, **567**, 66–70.

4 B. Kirubasankar, Y. S. Won, L. A. Adofo, S. H. Choi, S. M. Kim and K. K. Kim, *Chem. Sci.*, 2022, **13**, 7707–7738.

5 M. J. Shearer, L. Samad, Y. Zhang, Y. Zhao, A. Puretzky, K. W. Eliceiri, J. C. Wright, R. J. Hamers and S. Jin, *J. Am. Chem. Soc.*, 2017, **139**, 3496–3504.

6 L. Liu, Y. Sun, X. Cui, K. Qi, X. He, Q. Bao, W. Ma, J. Lu, H. Fang, P. Zhang, L. Zheng, L. Yu, D. J. Singh, Q. Xiong, L. Zhang and W. Zheng, *Nat. Commun.*, 2019, **10**, 4472.

7 C. C. Lu, Y. C. Lin, Z. Liu, C. H. Yeh, K. Suenaga and P. W. Chiu, *ACS Nano*, 2013, **7**, 2587–2594.

8 Y. Cao, V. Fatemi, A. Demir, S. Fang, S. L. Tomarken, J. Y. Luo, J. D. Sanchez-Yamagishi, K. Watanabe,

T. Taniguchi, E. Kaxiras, R. C. Ashoori and P. Jarillo-Herrero, *Nature*, 2018, **556**, 80–84.

9 T. Cea, N. R. Walet and F. Guinea, *Nano Lett.*, 2019, **19**, 8683–8689.

10 Y. P. Yang, J. D. Li, J. Yin, S. G. Xu, C. Mullan, T. Taniguchi, K. Watanabe, A. K. Geim, K. S. Novoselov and A. Mishchenko, *Sci. Adv.*, 2020, **6**, eabd3655.

11 K. Liu, L. Zhang, T. Cao, C. Jin, D. Qiu, Q. Zhou, A. Zettl, P. Yang, S. G. Louie and F. Wang, *Nat. Commun.*, 2014, **5**, 4966.

12 L. Sun, Z. Wang, Y. Wang, L. Zhao, Y. Li, B. Chen, S. Huang, S. Zhang, W. Wang, D. Pei, H. Fang, S. Zhong, H. Liu, J. Zhang, L. Tong, Y. Chen, Z. Li, M. H. Rümmeli, K. S. Novoselov, H. Peng, L. Lin and Z. Liu, *Nat. Commun.*, 2021, **12**, 2391.

13 Y. Yu, G. S. Jung, C. Liu, Y. C. Lin, C. M. Rouleau, M. Yoon, G. Eres, G. Duscher, K. Xiao, S. Irle, A. A. Puretzky and D. B. Geohegan, *ACS Nano*, 2021, **15**, 4504–4517.

14 M. J. Bierman, Y. K. Lau, A. V. Kvit, A. L. Schmitt and S. Jin, *Science*, 2008, **320**, 1060–1063.

15 J. Zhu, H. Peng, A. F. Marshall, D. M. Barnett, W. D. Nix and Y. Cui, *Nat. Nanotechnol.*, 2008, **3**, 477–481.

16 Y. Liu, J. Wang, S. Kim, H. Sun, F. Yang, Z. Fang, N. Tamura, R. Zhang, X. Song, J. Wen, B. Z. Xu, M. Wang, S. Lin, Q. Yu, K. B. Tom, Y. Deng, J. Turner, E. Chan, D. Jin, R. O. Ritchie, A. M. Minor, D. C. Chrzan, M. C. Scott and J. Yao, *Nature*, 2019, **570**, 358–362.

17 Z. Song, X. Sun and L.-W. Wang, *Phys. Rev. B*, 2021, **103**, 245206.

18 H. H. Teng, P. M. Dove and J. J. De Yoreo, *Geochim. Cosmochim. Acta*, 2000, **64**, 2255–2266.

19 I.V. Markov, *Crystal Growth For Beginners: Fundamentals of Nucleation, Crystal Growth, and Epitaxy*, World Scientific Publishing Co. Pte. Ltd, 1st edn, 1995.

20 W. K. Burton, N. Cabrera and F. C. Frank, *Philos. Trans. R. Soc. London*, 1951, **243**, 299–358.

21 F. Meng, S. A. Morin, A. Forticaux and S. Jin, *Acc. Chem. Res.*, 2013, **46**, 1616–1626.

22 S. A. Morin, A. Forticaux, M. J. Bierman and S. Jin, *Nano Lett.*, 2011, **11**, 4449–4455.

23 L. Chen, B. Liu, A. N. Abbas, Y. Ma, X. Fang, Y. Liu and C. Zhou, *ACS Nano*, 2014, **8**, 11543–11551.

24 H. J. Park, R. Y. Tay, X. Wang, W. Zhao, J. H. Kim, R. S. Ruoff, F. Ding, E. H. T. Teo and Z. Lee, *Nano Lett.*, 2019, **19**, 4229–4236.

25 L. Zhang, K. Liu, A. B. Wong, J. Kim, X. Hong, C. Liu, T. Cao, S. G. Louie, F. Wang and P. Yang, *Nano Lett.*, 2014, **14**, 6418–6423.

26 A. Zhuang, J. J. Li, Y. C. Wang, X. Wen, Y. Lin, B. Xiang, X. Wang and J. Zeng, *Angew. Chem., Int. Ed.*, 2014, **53**, 6425–6429.

27 A. Forticaux, L. Dang, H. Liang and S. Jin, *Nano Lett.*, 2015, **15**, 3403–3409.

28 X. Fan, Y. Zhao, W. Zheng, H. Li, X. Wu, X. Hu, X. Zhang, X. Zhu, Q. Zhang, X. Wang, B. Yang, J. Chen, S. Jin and A. Pan, *Nano Lett.*, 2018, **18**, 3885–3892.

29 Y.-R. Chang, N. Higashitarumizu, H. Kawamoto, F.-H. Chu, C.-J. Lee, T. Nishimura, R. Xiang, W.-H. Chang, S. Maruyama and K. Nagashio, *Chem. Mater.*, 2020, **33**, 186–194.

30 Y. Zhao, C. Zhang, D. D. Kohler, J. M. Scheeler, J. C. Wright, P. M. Voyles and S. Jin, *Science*, 2020, **370**, 442–445.

31 Y. Zhao and S. Jin, *Acc. Mater. Res.*, 2022, **3**, 369–378.

32 D. M. Huang, X. Wu, K. Chang, H. Hu, Y. L. Wang, H. Q. Xu and J. J. Zhang, *Adv. Sci.*, 2023, **10**, e2301326.

33 K. Momma and F. Izumi, *J. Appl. Crystallogr.*, 2008, **41**, 653–658.

34 G. Kresse and J. Furthmüller, *Comput. Mater. Sci.*, 1996, **6**, 15–50.

35 J. P. Perdew, K. Burke and M. Ernzerhof, *Phys. Rev. Lett.*, 1996, **77**, 3865–3868.

36 P. E. Blochl, *Phys. Rev. B:Condens. Matter Mater. Phys.*, 1994, **50**, 17953–17979.

37 D. Sheppard, P. Xiao, W. Chemelewski, D. D. Johnson and G. Henkelman, *J. Chem. Phys.*, 2012, **136**, 074103.

38 G. Henkelman, *J. Chem. Phys.*, 2000, **136**, 150901.

39 R. D. Bringans, R. I. G. Uhrberg, R. Z. Bachrach and J. E. Northrup, *J. Vac. Sci. Technol., A*, 1986, **4**, 1380–1384.

40 X. Lin, J. C. Lu, Y. Shao, Y. Y. Zhang, X. Wu, J. B. Pan, L. Gao, S. Y. Zhu, K. Qian, Y. F. Zhang, D. L. Bao, L. F. Li, Y. Q. Wang, Z. L. Liu, J. T. Sun, T. Lei, C. Liu, J. O. Wang, K. Ibrahim, D. N. Leonard, W. Zhou, H. M. Guo, Y. L. Wang, S. X. Du, S. T. Pantelides and H. J. Gao, *Nat. Mater.*, 2017, **16**, 717–721.

41 Y. Cai, Q. Ke, G. Zhang, B. I. Yakobson and Y. W. Zhang, *J. Am. Chem. Soc.*, 2016, **138**, 10199–10206.

42 A. A. Kistanov, D. R. Kripalani, Y. Cai, S. V. Dmitriev, K. Zhou and Y.-W. Zhang, *J. Mater. Chem. A*, 2019, **7**, 2901–2907.

43 A. A. Kistanov, Y. Cai, D. R. Kripalani, K. Zhou, S. V. Dmitriev and Y.-W. Zhang, *J. Mater. Chem. C*, 2018, **6**, 4308–4317.

44 T. Akiyama and T. Kawamura, *Phys. Status Solidi B*, 2024, **261**, 2300573.

45 P. Xiao, Y. Chen, F. Chen, W. Liu, J. Han, L. Qiao, J. Li, L. Zhao, T. Song, Z. Wang and W. Xiao, *J. Phys. Chem. Lett.*, 2024, **15**, 6415–6423.

46 X. Zhou, Y. Liang, H. Fu, R. Zhu, J. Wang, X. Cong, C. Tan, C. Zhang, Y. Zhang, Y. Wang, Q. Xu, P. Gao and H. Peng, *Adv. Mater.*, 2022, **34**, 2202754.

47 Y. Li, Y. Wu and S. Ding, *Phys. B*, 2022, **627**, 413528.

48 D. R. Kripalani, A. A. Kistanov, Y. Cai, M. Xue and K. Zhou, *Phys. Rev. B*, 2018, **98**, 085410.